13th International Symposium on Particle Image Velocimetry – ISPIV 2019
Munich, Germany, July 22-24, 2019

Volumetric Measurement of Synthetic Jet Impingement with Single-camera Light-field PIV

Junfei Ding[1], Shengming Xu[1], Zhou Zhao[1], Shengxian Shi[1*], Rene Kaufmann[2], Bharathram Ganapathisubramani[2*]

[1]Shanghai Jiao Tong University, School of Mechanical Engineering, Shanghai, China

[2] University of Southampton, Faculty of Engineering and the Environment, Southampton, UK

*kirinshi@sjtu.edu.cn

*G.Bharath@soton.ac.uk

Abstract

The periodic ingestion and ejection of fluid through an orifice yield vortex rings forming an unsteady jet. The ability to impart momentum with a zero net mass flux makes synthetic jet actuators coveted components in flow control applications. When the geometry of the orifice is slit, the flow field has more obvious 3D characteristics. The purpose of this research is to experimentally study the flow characterization of an impinging synthetic jet with split orifice measured by phase locked single-camera light-field PIV (LF-PIV), which as a novel 3D-3C PIV technique has been successfully applied to several 3D-3C flow measurement studies. The jet is generated by a reciprocating loudspeaker which actuated with a sinusoidal voltage signal in cavity behind a split orifice with size $d \times l$ ($d = 1mm$, $l = 8mm$). 100 instantaneous 3D-3C velocity are measured in each phase of 20 phases. The features of the mean flow quantities and its turbulent statistics are described with triple decomposition analysis.

1 Introduction

Synthetic jets are generated by fluids pushed through an orifice into a chamber with no net mass flow through the orifice. Equal amount of suction pulse will follow the blowing pulse meaning that synthetic jets are formed entirely from the working fluid (Smith and Glezer, 1998). Reduplicative blowing pulses are created by periodic oscillation of dynamic actuators that encloses a cavity behind the orifice (Rizzetta D et al. 1999). With a fixed oscillation frequency, a series of vortex rings will propagate downstream and break down somewhere away from the orifice, thus forming a turbulent jet (Holman R et al. 2005). One reason for the study of such vortices and their interactions is the believed existence of coherent structures in many types of turbulent flow and the idea where turbulence can be represented as a superposition of interacting vortices (Saffman P and Baker GR 1979).

The intention of this paper will be focused on volumetric study of both self-induced and synergistic flow structure of synthetic jets by applying three-dimensional light-field PIV. Theoretical and practical researches have been conducted upon light-field PIV by Fahringer TW et al. (2015) and Shi S et al. (2016, 2018). This technique is capable of resolving 3D velocity field, and has been successfully applied in several experimental studies such as supersonic jet (Ding J et al. 2018) and in a single-fin SBLI by Jones C (2018).

2 Theoretical Considerations and Parameterization

2.1 Governing parameters

While describing the behavior of synthetic jets, some assumptions need to be made. Firstly, it is inferred that the velocity of the jet is constant over the exit plane due to the simple top-hat velocity profile at the orifice exit. Although this overestimates the spatial velocity and the total mass flow at most locations of the jet exit (Feero et al. 2015), measurements performed by Smith and Glezer (2005) and Aydemir et al. (2012) support the above approximation and show that the jet centerline velocity at the orifice exit follows a sinusoidal profile, given by

$$u(t) = u_{max} sin(\frac{2\pi t}{\tau} + \theta) \tag{1}$$

where u_{max}, $t(s)$ and $\tau(s)$ represents the maximum velocity during the blowing cycle, the time and the period of the cycle, respectively. Further, following Smith and Glezer (1998), the mean blowing velocity, $\bar{u}$, is used as a representative velocity throughout and is defined as

$$\bar{u} = \frac{1}{\tau}\int_0^{\tau/2} u(t)\mathrm{d}t = \frac{1}{\tau}\int_0^{\tau/2} u_{max} sin(\frac{2\pi t}{\tau})\ \mathrm{d}t = \frac{u_{max}}{\pi} \tag{2}$$

The flow of a single synthetic jet can be characterized using three dimensionless parameters (Glezer and Amitay, 2002): the aspect ratio, the Strouhal number and the Reynolds number, defined as

$$AR = \frac{l}{d} \tag{3}$$

$$Sr = \frac{fd}{\bar{u}} = \frac{d}{Lo} \tag{4}$$

$$Re = \frac{\bar{u}d}{\nu} \tag{5}$$

Where ν is the fluid kinematic viscosity, $f = 1/\tau$ is the actuation frequency and Lo is the stroke length, defined as $\bar{u}/f$.

2.2 Triple Decomposition

The instantaneous velocity data, obtained through the MCCDPIV algorithm, is analysed using triple decomposition (Hussain & Reynolds 1970; Kitsios et al. 2010; Soria 2015):

$$u_i(\boldsymbol{x}, t) = U_i(\boldsymbol{x}) + \tilde{u}_i(\boldsymbol{x}, t) + u_i'(\boldsymbol{x}, t) \tag{6}$$

where $u_1 = u$, $u_2 = v$,$u_3 = w$, $\boldsymbol{x} = (X, Y, Z)$, U_i is the time-average velocity, $\tilde{u}_i$ is the phase-correlated organized contribution to the velocity and u_i' is the turbulent velocity fluctuation. The time-average velocity is defined as

$$U_i(\boldsymbol{x}) = \lim_{T\to\infty} \frac{1}{T}\int_0^T u_i(\boldsymbol{x}, t)\mathrm{d}t \tag{7}$$

Where $U_1 = U, U_2 = V, U_3 = W$. while the phase-average velocity is

$$\langle u_i(\boldsymbol{x}, t)\rangle = \lim_{N\to\infty} \frac{1}{N}\sum_{n=0}^{N-1} u_i(\boldsymbol{x}, t + n\tau) \tag{8}$$

where N is the number of snapshots of the flow fields at the same phase, and n is a natural number. Hence the phase-average velocity is the average in any spatial point for a fixed phase t/τ in the synthetic jet generation cycle. The phase-correlated organized contribution to the velocity is thus defined as

$$\tilde{u}_i(\boldsymbol{x}, t) = \langle u_i(\boldsymbol{x}, t)\rangle - U_i(\boldsymbol{x}) \tag{9}$$

while the turbulent velocity fluctuation is

$$u_i'(\boldsymbol{x}, t) = u_i(\boldsymbol{x}, t) - \langle u_i(\boldsymbol{x}, t)\rangle \tag{10}$$

In the time-average behaviour of the impinging ZNMF jet flow field, the kinetic energy is due to three contributions: the mean kinetic energy ($\propto \sum_{i=1}^{2} {U_i}^2$), the phase-correlated kinetic energy (PKE) and the turbulent kinetic energy (TKE). The second one is generated by the periodic external force, perturbing the flow field, and is defined as

$$PKE(\boldsymbol{x}) = \sum_{i=1}^{3}\left[\lim_{T\to\infty}\frac{1}{T}\int_0^T \tilde{u}_i^2(\boldsymbol{x},t)\mathrm{d}t\right] \quad (11)$$

While the third one is the kinetic energy related to the turbulence and is defined as usual as

$$TKE(\boldsymbol{x}) = \sum_{i=1}^{3}\left[\lim_{T\to\infty}\frac{1}{T}\int_0^T u_i'^2(\boldsymbol{x},t)\mathrm{d}t\right] \quad (12)$$

2.3 Vorticity

The 3D vorticity $(\omega_x, \omega_y, \omega_z)$ is defined as

$$\omega_x = \frac{\partial w}{\partial y} - \frac{\partial v}{\partial z} \quad (13)$$

$$\omega_y = \frac{\partial u}{\partial z} - \frac{\partial w}{\partial x} \quad (14)$$

$$\omega_z = \frac{\partial v}{\partial x} - \frac{\partial u}{\partial y} \quad (15)$$

It is calculated by using the PIV velocity field measurements through a local least squares fitting procedure to the velocity field.

3 Experimental setup and procedures

A schematic of the impinging synthetic jet experimental setup is presented in Fig. 1. A Visaton SC 8N speaker is used to actuate the synthetic jet actuator. This speaker has an impedance of 8Ω with a rated power of 30W (corresponding to $A = 15$Vpp) and a frequency response between 70-20000 Hz. Therefore, the synthetic jet actuator is operated with an amplitude limit of $A = 15$Vpp and a lower frequency limit of $f = 100$Hz. The average blowing velocity of the synthetic jet actuator is measured for multiple amplitudes and frequencies. The operating conditions for this paper is $A = 15$Vpp and $f = 100$Hz, corresponding $Sr = 0.0117$, $Re = 548$ and $Lo = 0.08545$.

The slot width is $d = 1mm$, and the slot length is $l = 8mm$, resulting in an aspect ratio of $AR = 13$. The actuators are milled from aluminium plates with 3D printed nozzles. The accuracy of the 3D printing technique is 0.1 mm. The actuators are flush mounted in a horizontal plate, with the slot exits perpendicular to the plate. The actuators have a volume of $1.85 \times 10^{-5}m^3$ and a neck length of $l_{neck} = 19.5$ mm. The orifice-to-plate distance is $24d$.

Measurements are performed using phase lock single-camera Light-field particle image velocimetry (LF-PIV). The smoke box is seeded with Pro Smoke Super particles with a nominal diameter of 1 μm, that generated by Martin MAGNUM 1200 smoke machine. The measurement volume was illuminated with a double pulse 500 mJ/pulse Nd:YAG laser (Litron), and the laser beam formed using two cylindrical convex lens and two cylindrical concave lenses. An in-house plenoptic PIV camera (6600 × 4400 pixel, *Shi et al. 2016*) was used to capture the field of view whose size is $36 \times 22 \times 11d$ located$1d$ above the orifice center. The laser and the camera are phase-locked to the driving signal using a National Instruments NI-DAQ. 100 LF-PIV image pairs were captured at a rate of 1 frame pairs/s for each phase of 20 phases.

4 Results and Discussion

In this section the experimental results are presented and discussed with a description of the statistics of the velocity and azimuthal vorticity from the triple decomposition of the 3D-3C velocity fields, (u, v, w), which is triple decomposed following the definition given in Eq.(6). The vorticity$(\omega_x, \omega_y, \omega_z)$ has an analogous triple decomposition.

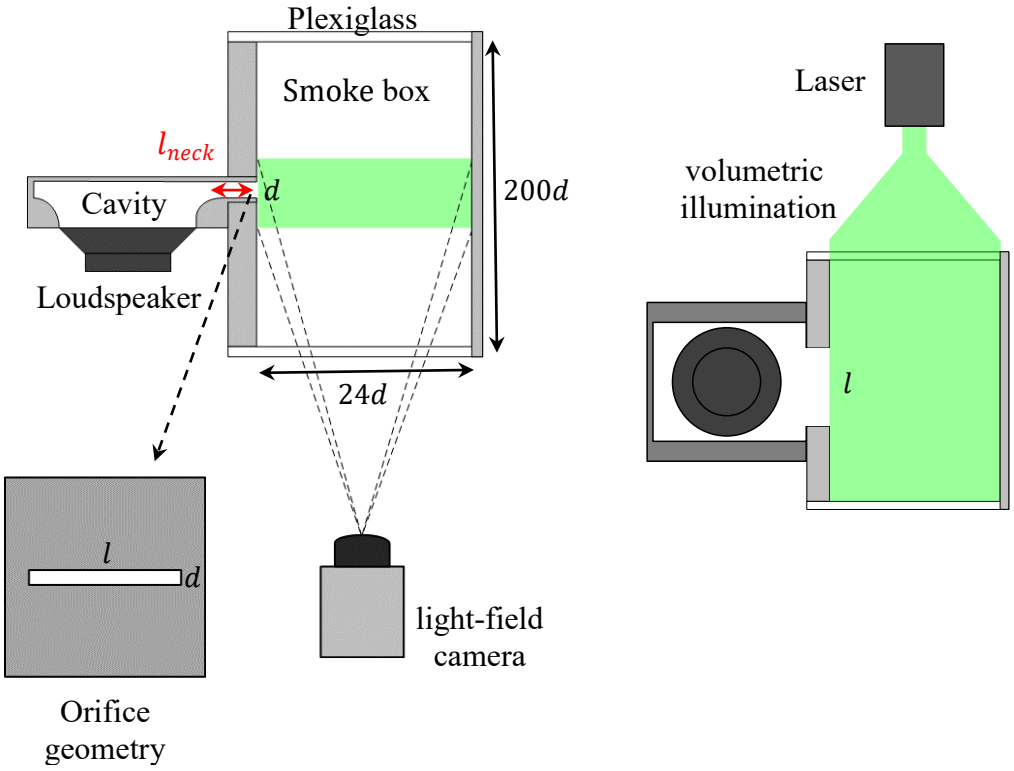

Figure 1: schematic of the impinging synthetic jet experimental setup.

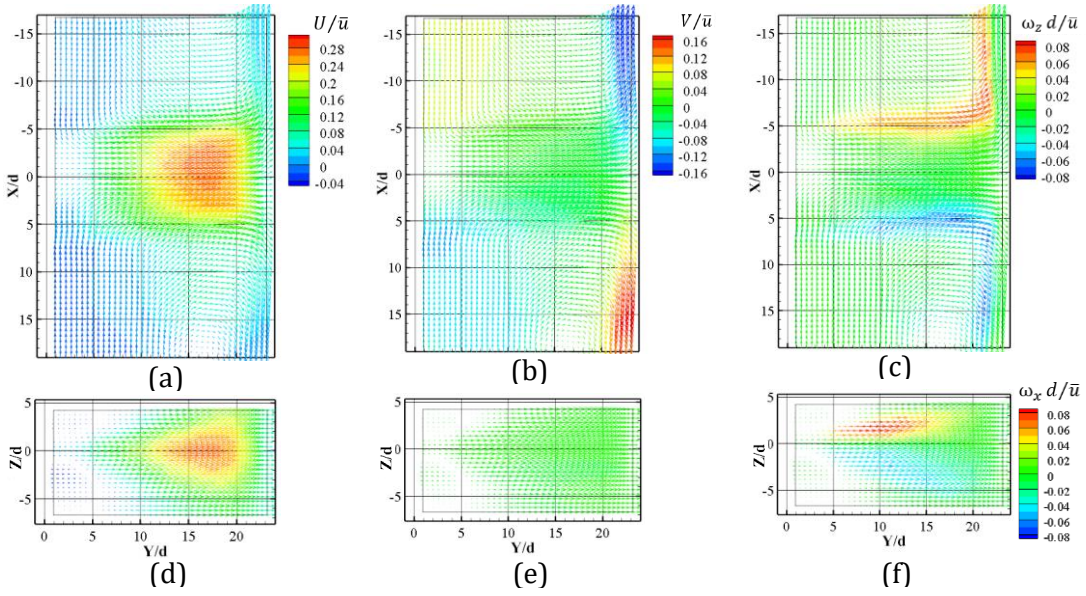

Figure 2: Time averaged mean velocity vector field. (a) and (d) axial velocity, $V/\bar{u}$, maps in $Z/d = 0$ slice of x-y view and in $X/d = 0$ slice of z-y view, respectively, (b) and (e) radial velocity in x-direction, $U/\bar{u}$, maps in $Z/d = 0$ slice of x-y view and in $X/d = 0$ slice of z-y view, respectively, (c) z-direction vorticity, $\omega_z \times d/\bar{u}$, maps in $Z/d = 0$ slice of x-y view, (f) x-direction vorticity, $\omega_x \times d/\bar{u}$, maps in $X/d = 0$ slice of z-y view.

Figure 2 shows the time averaged mean velocity field for the domain of the impinging synthetic jet of interest. The maps of axial velocity, $V/\bar{u}$, in slice Z/d=0 and in slice in X/d=0 is shown in (a) and (c) respectively. And The maps of radial velocity $U/\bar{u}$ in slice Z/d=0 and in slice in X/d=0 is shown in (b) and (d) respectively. Figure 2 (c) shows z-direction vorticity $\omega_z \times d/\bar{u}$ maps in $Z/d = 0$ slice and Figure 2 (f) shows x-direction vorticity $\omega_x \times d/\bar{u}$ maps in slice $X/d = 0$. These measurements have been used to extract the variation with axial direction, y, of the mean axial centerline velocity, $V_c(y)$ as shown in Fig. 3 and the half width of the mean axial velocity profile of the impinging synthetic jet, $r_{1/2}(x, y, z)$, which is defined as the radius where the mean axial velocity has decayed from its centerline value by half, as shown in Fig. 4. The geometry of $r_{1/2}(x, y, z)$ surface is found to change from slit to circle with the distance far away from orifice.

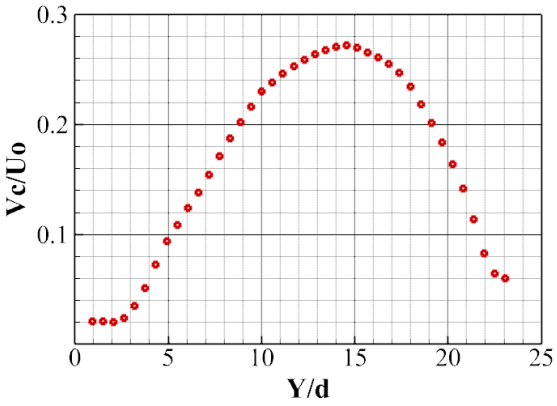

Figure 3: Axial mean center-line velocity, $V_c(y)/\bar{u}$, variation with axial direction y.

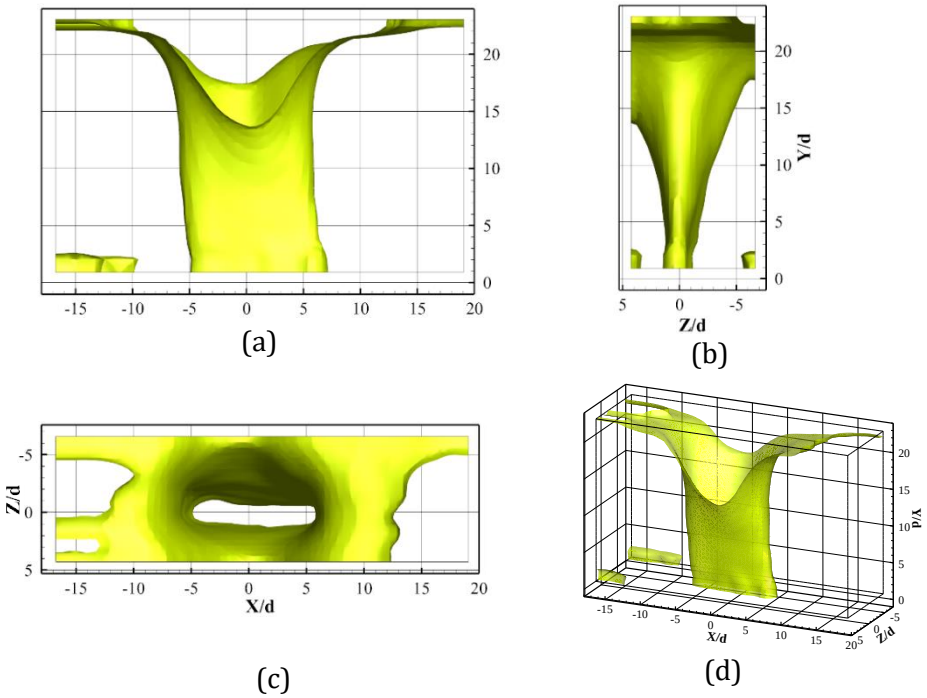

Figure 4: Half-width surface, $r_{1/2}(x, y, z)$, variation with axial direction y. (a)(b)and(c) shown in x-y view, y-z view and top view respectively, (d) shown in 3D view.

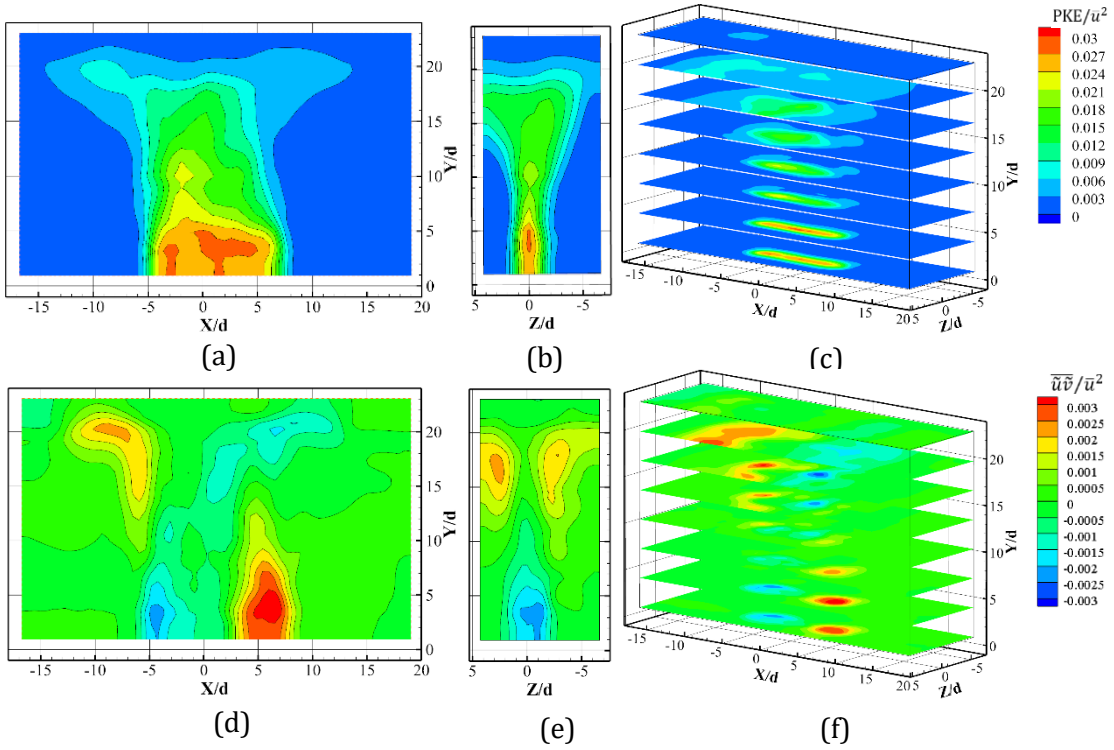

Figure 5: The colour range represents in: (a)(b)and (c) Time average phase correlated kinetic energy maps in x-y view, z-y view and 3D view, respectively, and (d)(e)and (f) Time average phase correlated organized contribution to the velocity Reynolds stress maps in x-y view, z-y view and 3D view, respectively.

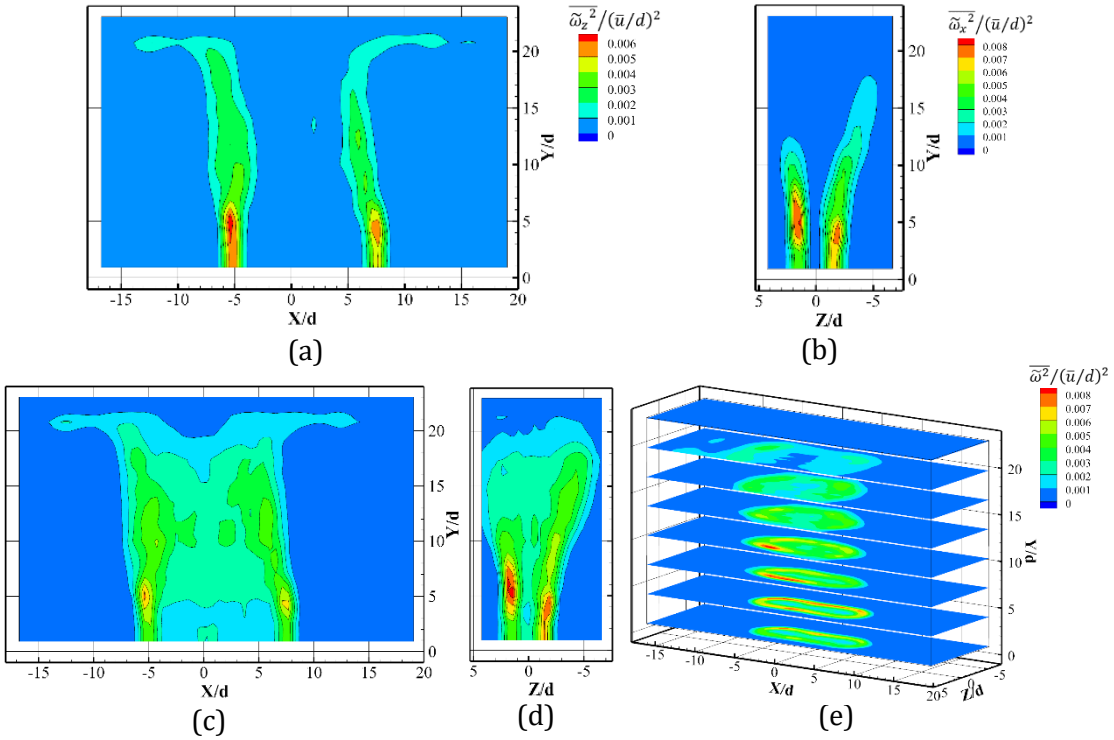

Figure 6: The colour range represents in: phase correlated mean square vorticity oscillations (a) $\overline{\tilde{\omega}_z{}^2}/(\bar{u}/d)^2$, (b) $\overline{\tilde{\omega}_x{}^2}/(\bar{u}/d)^2$, (c)(d)and (e) $\overline{\tilde{\omega}^2}/(\bar{u}/d)^2$, respectively.

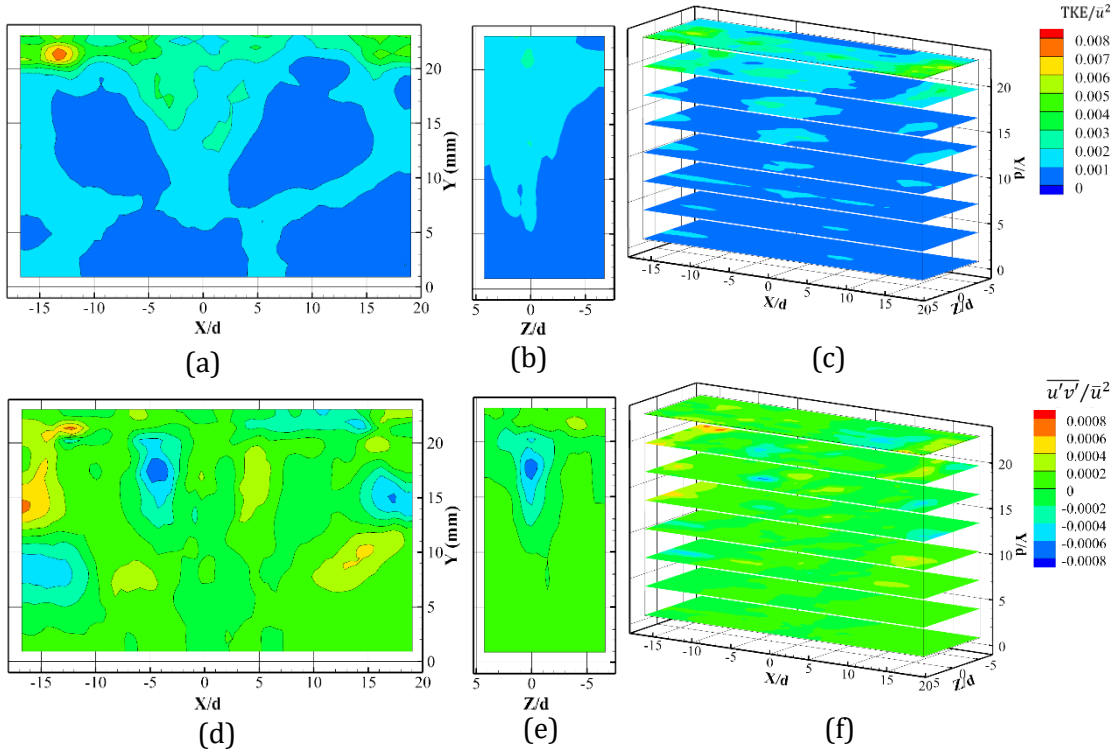

Figure 7: The colour range represents in: (a)(b)and (c) Time average turbulent kinetic energy maps in x-y view, z-y view and 3D view, respectively, and (d)(e)and (f) Time average turbulent Reynolds stress maps in x-y view, z-y view and 3D view, respectively.

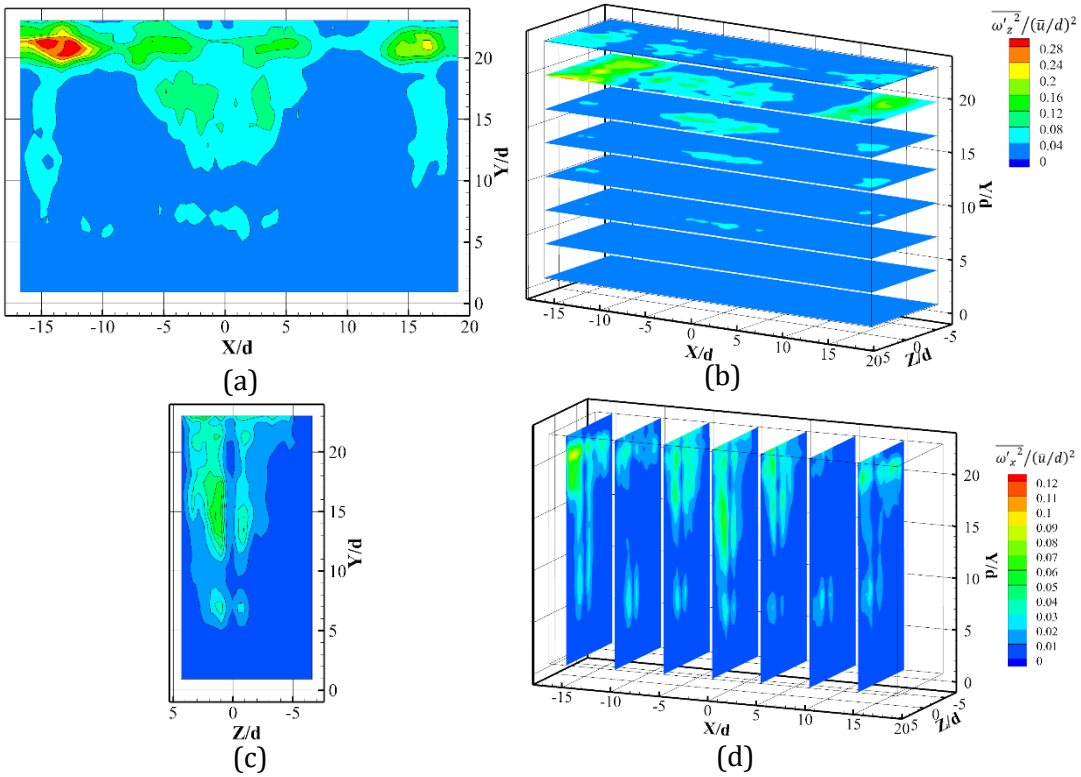

Figure 8: The colour range represents in: time average turbulent mean square vorticity oscillations (a)(b) $\overline{\omega'_z{}^2}/(\bar{u}/d)^2$, (c)(d) $\overline{\omega'_x{}^2}/(\bar{u}/d)^2$, respectively.

The maps of the second order statistics of the time-dependent triple decomposition components of 3D velocity and vorticity are shown in Figure 5-8, respectively. The time average phase correlated kinetic velocity maps are depicted in Fig. 5(a)(b) and (c). It is possible to highlight that the maximum value is attained on the orifice exit. Time average phase organized contribution to the velocity Reynolds stress shows (in Fig. 5(d)(e) and (f)) its maximum value, near the orifice and the impinging plate, at corresponding to the Half-width surface. The phase correlated mean square vorticity oscillations maps are depicted in Fig. 6. In Fig. 7(a)(b) and (c), the time average turbulent kinetic energy maps are reported. For each configuration the maximum values are concentrate on impinging part. Hence the vortex ring has higher turbulent value and stays more time near the impinging plate causing such a region. The phase correlated mean square vorticity oscillations maps are depicted in Fig. 8.

5 Conclusion

This study presents the flow characteristic of an impinging synthetic jet with an aspect ratio 8 slit orifice. The phase lock LF-PIV was used to reconstruct 3D-3C velocity of 20 phases. The features of the mean flow quantities and its turbulent statistics are described with triple decomposition analysis.

Acknowledgements

The authors are grateful to the Southampton University for facilitating the experiments.
This work is supported by the National Natural Science Foundation of China (Grant No.11472175, No.11772197).

References

Aydemir E, Worth NA, Dawson JR (2012) The formation of vortex rings in a strongly forced round jet. *Experiments in Fluids*, 52:729–742

Berk T, Hutchins N, Marusic I, and Ganapathisubramani B (2018) Trajectory of a synthetic jet issuing into high-Reynolds-number turbulent boundary layers. *Journal of Fluid Mechanics*, 856:531-551

Ding J, Lim HD, Sheikh S, Xu S, Shi S, and New TH (2018) Volumetric Measurement of a Supersonic Jet with Single-Camera Light-Field PIV. *19th International Symposium on the Application of Laser and Imaging Techniques to Fluid Mechanics, Lisbon, Portugal, July 16-19, 2018*

Fahringer T, Lynch KP, and Thurow B (2015). Volumetric particle image velocimetry with a single plenoptic camera. *Measurement Science and Technology*, 26:115201

Feero MA, Lavoie P, Sullivan PE (2015) Influence of cavity shape on synthetic jet performance. *Sensors and Actuators A: Physical*, 223:1–10

Glezer A, Amitay M (2002) Synthetic Jets. *Annual review of fluid mechanics*, 34:503–529

Jones C, Clifford C, Thurow B, Mears L, Arora N, and Alvi F (2018). Plenoptic PIV Applied to 3D Single-Fin SBLI With and Without Flow Actuation. *71st Annual Meeting of the APS Division of Fluid Dynamics, Atlanta, Georgia, November 18–20, 2018*

Rizzetta DP, Visbal MR, and Stanek MJ (1999) Numerical investigation of synthetic-jet flowfields. *AIAA journal*, 37:919-927

Saffman PG, and Baker GR (1979). Vortex interactions. *Annual Review of Fluid Mechanics*, 11:95-121

Shi S, Wang J, Ding J, Zhao Z, and New TH (2016) Parametric study on light field volumetric particle image velocimetry. *Flow Measurement and Instrumentation*, 49:70-88

Shi S, Ding J, Atkinson C, Soria J, and New TH (2018) A detailed comparison of single-camera light-field PIV and tomographic PIV. *Experiments in Fluids*, 59:46

Smith BL, and Glezer A (1998) The formation and evolution of synthetic jets. *Physics of fluids*, 10:2281-2297

Smith BL, and Glezer A (2005) Vectoring of adjacent synthetic jets. *AIAA journal*, 43:2117–2124